SOAR Adaptive Module (SAM): seeing improvement with a UV laser

7 authors, including:

Andrei Tokovinin
National Optical Astronomy Observatory
286 PUBLICATIONS   **3,894** CITATIONS

SEE PROFILE

Rolando Cantarutti
National Optical Astronomy Observatory
15 PUBLICATIONS   **84** CITATIONS

SEE PROFILE

Roberto Tighe
National Optical Astronomy Observatory
25 PUBLICATIONS   **124** CITATIONS

SEE PROFILE

SOAR ADAPTIVE MODULE (SAM): SEEING IMPROVEMENT WITH A UV LASER

Andrei Tokovinin, Rolando Cantarutti, Roberto Tighe, Patricio Schurter, Manuel Martinez, Sandrine Thomas[1], Nicole van der Bliek,

Cerro Tololo Inter-American Observatory, Casilla 603, La Serena, Chile

Draft version August 22, 2016

ABSTRACT

The adaptive module of the 4.1-m SOAR telescope, SAM, corrects ground-layer turbulence using a UV laser guide star. It has been commissioned in 2013 and it is in regular science operation since 2014. SAM works with the CCD imager covering a 3′ field or with the speckle camera. It operates routinely and stably, delivering resolution in the I band equal to the free-atmosphere seeing. This paper describes the SAM system as a whole, providing essential reference for its users and technical information of interest to instrumentalists. Operation of the instrument, its performance, and science projects done with SAM so far are reviewed.

Subject headings: Astronomical Instrumentation, Adaptive Optics

1. INTRODUCTION

SOAR Adaptive Module (SAM) is a facility adaptive optics (AO) instrument at the 4.1-m Southern Astrophysical Research Telescope, SOAR. It improves the natural seeing by partial compensation of turbulence near the ground. Although various aspects of SAM have been covered in the literature, there has been no single reference with a comprehensive description of the entire instrument and its performance. The present article fills this lacuna. It is primarily intended for SAM users and may be of interest to instrument developers. On the other hand, the format of a journal article is not well suited for technical details such as full optical prescription, software algorithms, etc.; this paper is *not* an instrument reference manual.

From the outset, the SOAR telescope was designed to deliver high angular resolution over a relatively narrow field, unlike other wide-angle 4-m telescopes (Sebring et al. 2002). It contains a fast actuated tertiary mirror (M3) for compensation of atmospheric tilts. Extending the compensation order using the AO technology appeared natural. However, SOAR is used mostly at visible wavelengths, where the standard AO compensates turbulence only over a narrow few-arcsec field and needs a bright star or a powerful laser to do so. In 2002, when SOAR was completed, the AO technology enabled good turbulence correction only in the infrared (IR). However, low-order IR AO systems still provided *partial* correction in the visible and could improve the resolution by a factor of ~ 2, as demonstrated by the PUEO instrument (Rigaut et al. 1998). Such partial correction could benefit a large range of science projects done at SOAR at visible wavelengths.

The idea of correcting only low-altitude turbulence, known as Ground-Layer AO (GLAO), was first formulated by Rigaut (2002). In GLAO, the compensation quality is traded against uniformity of correction over a wide field. Quantitative analysis of GLAO was done later by Tokovinin (2004), see also Andersen et al. (2006). Although several natural guide stars (NGSs) or laser guide stars (LGSs) located at the perimeter of the field of view

are optimal for sensing ground-layer turbulence, even a single LGS at low altitude is an acceptable solution for GLAO. In such case, the so-called cone effect effectively reduces sensitivity to high-altitude turbulence.

The concept of SAM, first presented by Tokovinin et al. (2003), is based on a single LGS created by Rayleigh scattering of an ultraviolet (UV) laser. The use of a UV laser, advocated by Angel & Lloyd-Hart (2000), has several advantages: efficient Rayleigh scattering proportional to λ^{-4}, easy separation of the laser light from longer science wavelengths, and no ocular hazards, making the beam safe to airplanes. The LGS is needed for a high sky coverage; an alternative wave-front sensor (WFS) using several NGSs would deliver a much inferior compensation. At that time, an AO system with a UV laser was being built for the 2.5-m telescope at Mt. Wilson (Thompson & Teare 2002), while a similar AO instrument with a green Rayleigh laser was developed at the 4.2-m William Hershel telescope (Rutten et al. 2006). For technical reasons, those two projects have not produced any science results, but we learned from their experience. The GLAO system with a green Rayleigh laser at the 6.5-m MMT telescope (Hart et al. 2010) is not used in regular observing programs. On the other hand, the Robo-AO instrument with a UV laser at the Palomar 1.5-m telescope (Baranec et al. 2012) is highly productive (e.g. Law et al. 2014).

The SAM instrument design was driven by the science goal (improve seeing over a moderate field of view at optical wavelengths), availability of suitable technology (e.g. UV lasers and fast CCD detectors), and technological trade-offs. In the development of SAM, we tried to use commercial or otherwise proven components, whenever possible. New and/or critical elements were first prototyped and tested. We consulted with the AO team at the MMT telescope who generously shared their experience.

The SAM system as a whole is presented in § 2. The main AO module is described in § 3, the laser subsystem is covered in § 4. § 5 describes the SAM software, and § 6 provides information on the SAM performance. Science operation is covered in § 7. In § 8 we discuss the place of SAM among other ground-based and space facilities, its future instruments and upgrades.

atokovinin@ctio.noao.edu

[1] AURA/LSST 950 N. Cherry Ave, Tucson AZ 85719, USA

2. SYSTEM ARCHITECTURE AND OVERVIEW

2.1. *Evolution of the concept*

The choice of the deformable mirror (DM) has a large impact on the instrument design. An adaptive secondary mirror, like in the MMT, would be an ideal technical solution, but it was beyond our budget and, in hindsight, would have substantially delayed the project. Initially we hoped to use a small electrostatic DM from OKO-tech and to build a small instrument around it, but the stroke of this DM turned out to be insufficient (Tokovinin et al. 2004b). We selected instead the bimorph DM BIM-60 made by CILAS. The initial optical relay based on refractive optics was replaced by a classical scheme with a pair of off-axis parabolic mirrors (OAPs) and a pupil diameter of 50 mm. Then the AO-corrected beam has the same focal ratio and pupil location as at the uncorrected telescope focus, allowing to use with SAM any instrument built for SOAR (within allowable mass and space limits). SAM acts as a seeing-improvement interface between SOAR and its science instrument. SAM feeds corrected images to its internal CCD detector, SAMI (4K×4K CCD) or to a visitor instrument (this port is now occupied by the speckle camera).

2.2. *System layout*
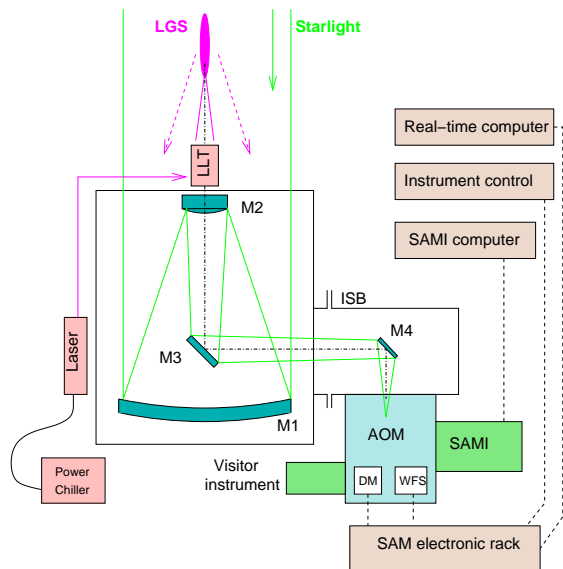
Figure 1. Simplified block-diagram of the SAM system. The science light path is denoted by green lines, the laser light path is in pink.

Figure 1 presents a simplified block-diagram of the SAM system. Light from celestial objects reflected by the SOAR primary mirror M1 experiences three more reflections before reaching the SAM Adaptive-Optics Module (AOM), attached to the instrument-selector box (ISB) at the Nasmyth focal station of SOAR. During observations, SAM rotates to compensate for parallactic angle. The optical relay inside AOM includes reflection from the DM. The corrected beam is sent either to SAMI or to the visitor instrument, both mounted on the opposite sides of the AOM.

The LGS is created by the pulsed UV laser located in a box on the telescope truss and also subjected to vari-

able gravity depending on the telescope elevation. The laser power supply and chiller are housed in a thermally insulated rack attached to the fork of the SOAR mount, in fixed gravity. The laser beam is transported to the laser launch telescope (LLT) located behind the SOAR secondary mirror, M2. Each pulse of the laser light propagates through the atmosphere and part of it is scattered back. Photons scattered from the distance of 7 km are selected by the fast range-gate shutter inside AOM, synchronized with the laser pulses. The UV light is analyzed by the WFS, and the correction is sent to the DM in closed loop. Other essential elements of SAM shown in Figure 1 are its electronics, mostly housed in a rack near the AOM, and its computers with software.

The Rayleigh scattering preserves polarization. The AOM rotates relative to the telescope and the laser, hence its polarization-sensitive WFS cannot be adjusted to match the polarization of the laser. To mitigate this effect, the laser beam is propagated circularly polarized, and the scattered circularly-polarized beam is converted back to linear polarization in the WFS. Only the oblique reflection from M3 slightly affects the polarization tuning.

SAM is different from the majority of AO systems in several ways. First, the tip and tilt (TT) compensation is provided by M3, the actuated tertiary mirror of SOAR, upstream from the instrument. Second, TT is sensed by two small guide probes deployed in the input (un-corrected) focal plane. This avoids the need to split photons in wavelength between science and guide channels. The probes sample the 5′ square patrol field outside the 3′ science field. In this design the tilts introduced by the deformable mirror (DM) are not sensed, but the DM control is tilt-free. The UV light from the LGS is focused well behind the nominal telescope focal plane, meaning that the light path of LGS photons inside SAM is very different from the starlight path. Nevertheless, major non-common-path errors between the science and WFS paths were avoided.

Readers who are not interested in the SAM design can skip the following material and go to Section 6.

3. ADAPTIVE OPTICS MODULE

In this Section, the AOM and its subsystems are covered.

3.1. *Optical relay*

The optical layout of the SAM AOM is shown in Figure 2, and the optical elements are listed in Table 1. The beam, focused by the telescope and reflected by the M4 mirror inside the ISB, propagates to the focal plane inside AOM, where guide probes (GPs) are located, and then hits the first OAP. Simulated light source can be inserted in the path before OAP1 for tests and DM flattening. The collimated beam after OAP1 propagates towards the DM, with an incidence angle of 14°.16. After the DM, the UV light is reflected by the dielectric coating of the dichroic plate, while longer wavelengths are transmitted through the dichroic towards OAP2 and refocused on the science instrument (after the fold mirrors). The SAMI fold mirror is installed permanently. The visitor fold mirror is mounted on a translation stage; when inserted, it intercepts the beam and directs it to the visitor port. The atmospheric dispersion corrector (ADC)
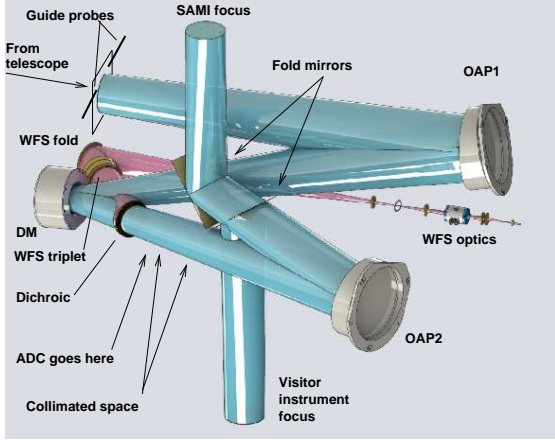
Figure 2. AOM optical layout. The beam corresponds to the circular field of $3'$ (60 mm) diameter.

can be inserted in the collimated beam after the dichroic. It consists of two cemented zero-deviation prisms, each made of the BaK2 (angle $4°45$) and CaF2 (angle $5°54$) glasses (Tighe et al. 2016). Immediately behind the ADC, the collimated space is available for insertion of other elements, for example a non-redundant pupil mask or a Fabry-Perot etalon.

The UV photons from the LGS at 7-km distance are focused well behind the science focal plane, very close to the OAP1. The LGS beam on the DM is divergent. Upon reflection from the dichroic, it is focused by the custom UV triplet lens, then the beam is folded by a mirror. The triplet also works well for the visible light, enabling SAM operation with the NGS. However, this mode was used only during initial commissioning, and SAM cannot be reconfigured back to work with NGS without losing the LGS capability.

The mirrors in the AOM, including the DM, have a protected silver coating with dielectric layers enhancing reflectivity at the laser wavelength 355 nm. The overall transmission in the science path was measured to be 0.90 at 633 nm. During optical integration, the Strehl ratio in the science channel at this wavelength reached 0.60 after alignment and with a carefully flattened DM. This means that, despite substantially different light path in the WFS, the non-common-path errors are not significant (remember that SAM optics does not need to be diffraction-limited).

The optical relay with two OAPs has a slightly curved field with a quadratic distortion. These effects, determined by the optical design, were confirmed by mapping the position and focus of the point light source. The curvature is small and it can be safely neglected, while the distortion is correctable by post-processing the images. The maximum lateral shift caused by the distortion is 0.6 mm or $1''8$.

3.2. *Deformable mirror*

SAM uses the bimorph or "curvature" DM BIM-60 made by the French company CILAS for the 8-m VLT telescope. The stroke of this DM is hence more than sufficient for the 4.1-m SOAR aperture, even considering the reduced pupil diameter of 50 mm instead of the nominal 60 mm. The curvature radius with a maximum voltage of 400 V on all electrodes is measured to be 6.7 m; a radius of 30 m would suffice to correct a $1''$ seeing in

SAM. The electrodes are arranged in radial geometry with five rings. Without any voltage, the DM has a large static aberration, including defocus. About half of the dynamic range is used to "flatten" the DM. The "flat" voltages depend on ambient temperature and instrument orientation, because the thin DM is deformed by gravity as SAM rotates, creating mainly defocus and trefoil. The gravity deformation is compensated by applying to all electrodes pre-calculated corrections varying as sines and cosines of the rotation angle. With those corrections, SAM can work in open loop, which is useful in its normal operation when the LGS is not needed or cannot be used for some reason.

Table 1
Optical elements of the SAM AOM

Element	Diam. (mm)	Dist. next (mm)	Notes
Common path			
Focal plane	60x60	810	Science field
OAP1	150	890	$F = 810$ mm
DM	60	150	BIM-60
Science path			
Dichroic	80	32	614.7 mm to OAP2
ADC prism1	80	3	Thickness 14.5mm
ADC prism2	80	550.6	Thickness 14.5mm
OAP2	150	345.5/455.5	To Visitor/SAMI
Visitor Fold	210x150	478.6	Visitor instrument
SAMI Fold	210x150	368.6	SAMI
Science focus	60x60	n/a	
WFS path			
Dichroic	80	180	
WFS triplet	80	65	UV triplet
WFS fold	100	616.3	Mirror
$\lambda/4$ plate	25	6.6	
F-adjuster lens	25	53.3	Single lens
Field stop	0.55x0.55	61.3	Square aperture
WFS collimator	25	10.2	Single lens
Polarizer-1	10	3	FocTek polarizer
Pockels cell	10	(20)	QX1020
Polarizer-2	10	10.2	FocTek polarizer
Re-imager L1	25	5.6	
Re-imager L2	25	43.3	
S-H focal plane	n/a	12.2	
S-H coll. lens	25	14.7	
Lenslet array	2.2	6.5	Pupil 1.989 mm
CCD-39	2.2	n/a	WFS detector

3.3. *Wavefront sensor*

SAM was first tested on the sky in 2009 with a simplified WFS, using an NGS for turbulence sensing. The UV dichroic was replaced then by a neutral beamsplitter. In the beginning of 2011, when SAM was finally commissioned in the NGS mode, the definitive LGS WFS was installed; it is described here. Both versions of the WFS used the same detector, CCD-39, and the same lenslet array (LLA).

The LGS WFS optics (Figure 3) is tailored to match the commercial Pockels cell QX1020 manufactured by Cleveland Crystals. Constraints on the beam angular divergence in the cell imposed by its birefringent material, KD*P, and the clear aperture of the cell, 10 mm, called for a $\sim$6-mm diameter beam inside the cell. So, after the field stop at the WFS focus the beam is colli-
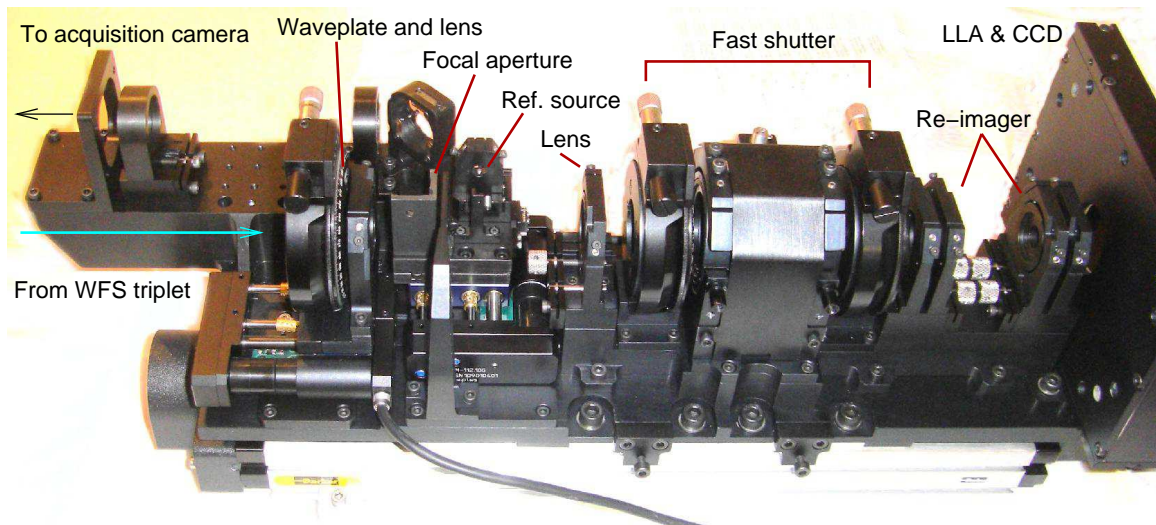
Figure 3. LGS WFS.

mated by a fused-silica lens (good for the monochromatic laser light). It passes through the first Glan-Taylor polarizer, the Pockels cell, and the second (crossed) polarizer. Then two more singlet lenses re-shape the beam and form the pupil image of 1.99 mm diameter on the LLA, to get 10×10 pupil sampling in the Shack-Hartmann WFS. The LLA is placed directly in front of the CCD. Its pitch, 0.192 mm, equals eight CCD pixels. The LLA focal length of 6.5 mm (at 633 nm) leads to the pixel scale of $0.''375$, and the field of view of $2.''8$, with 8 pixels per sub-aperture.

The optics of SAM allows the LGS distance to be set between 7 km and 14 km (it is fixed presently at 7 km). When the WFS is refocused to a different distance (it is mounted on a translation stage), the pupil size on the LLA changes slightly. To compensate for this variation, another weak singlet lens is placed before the focus on a small translation stage. Axial motion of this focal adjuster allows us to keep the constant pupil diameter at the LLA. The $\lambda/4$ wave plate is placed together with this lens to transform the elliptically polarized laser beam into linear polarization.

The parameters of the LLA APO-Q-P192-F5.75 were chosen optimally for the NGS WFS, while the second LLA with a shorter focal length of 3.17 mm was procured for the LGS WFS from the same vendor, $A\mu S$. Both LLAs are made of fused silica and have excellent optical quality. However, we could not use the short-focus LLA as planned because the distance from the CCD surface to its glass window exceeded the specification by 1 mm. To match the pixel scale and the size of the LGS spots, we bin the CCD 2×2, to $0.''75$ per binned pixel.

The CCD-39 detector has 80×80 pixels of $24\,\mu m$ size and four output amplifiers for fast readout. The vendor, e2v, guaranteed quantum efficiency of >0.4 at 355 nm. The detector is cooled thermoelectrically to about $-20°$C. CCD-39 works in SAM with the SDSU-III controller. With the 2×2 binning, the loop frequency is 478 Hz and the readout noise is about 5.5 electrons. The digitized signal is transmitted by the optical fiber from the controller to the acquisition board inside the real-time computer (RTC). The bias pattern is not very stable, requiring its re-calibration a few times per night,

while slow drifts of the bias in each quadrant are tracked and subtracted using signals in the empty corners of the image.

The duration of the range-gate pulse determines the vertical extent of the LGS and hence the maximum spot elongation in the peripheral sub-apertures. We normally use the 150-m range gate, or $1\,\mu s$ gate pulses. The amplitude of the driving pulses producing the $\lambda/2$ phase shift in the Pockels cell at the laser wavelength of 355 nm is 2.7 kV. The KD*P crystal in the cell is piezoelectric, so the driving pulses excite its acoustic oscillations at 95 kHz. As a result, the shutter does not close completely and some after-pulses or "ringing" appear. The $1\,\mu s$ drive pulses produce a spurious pulse of $\sim 10\%$ transmission delayed by $3.6\,\mu s$ from the opening edge of the gate. The weak "tails" of the LGS spots caused by this ringing are truncated by the WFS entrance aperture, except the innermost sub-apertures where they pass through and slightly bias the centroids.

The entrance aperture of the WFS is carefully aligned laterally to avoid "spilling" of light into adjacent sub-apertures. This aperture mask is mounted on a translation stage which, when moved, replaces it by a UV source used to measure the reference positions in each sub-aperture. At the same time the main beam is intercepted by a diagonal mirror that sends it to the acquisition camera. We use a simple GC650 CCD detector from Prosilica, with a Gigabit Ethernet interface, to acquire "live" image of the un-gated LGS. It is strongly peaked and easy to center.

3.4. *Tip-tilt guide probes*

Any LGS AO system needs a tip-tilt (TT) correction using natural guide stars because the LGS does not provide valid TT signal. In the case of GLAO, the requirements on residual TT errors are relaxed in comparison to the classical AO, as we do not need to reach the diffraction-limited resolution. However, the sky coverage is essential. Our calculations indicated that the faint limit of the TT probes should be no less than $R = 18$ mag for reaching the full sky coverage.

Atmospheric TT errors increase with increasing angular distance from the TT guide star (so-called tilt

anisoplanatism). The resulting PSF non-uniformity was a concern for SAM. We planned to have three guide probes (GPs) picking stars around the science field of view (FoV). Further study showed that with just two GPs the correction uniformity is almost as good, so SAM has two GPs, each patrolling half of the field. The technical FoV for picking the stars is $5' \times 5'$ square.

We take advantage of the SOAR fast tertiary mirror for the TT correction. The GPs are placed at the telescope focus upstream from the optical relay. To reduce vignetting, the width of the GPs is minimized to 6 mm. The optical scheme of the GPs is shown in Figure 4. The 2×2 array of 0.5-mm acrylic micro-lenses, cut from a larger sample, is optically coupled to four multimode fibers with a core diameter of $100\,\mu m$. The SOAR pupil image on the fiber ends has a diameter of $90\,\mu m$, allowing some tolerance for alignment. Each fiber, glued into a steel ferrule, is aligned with respect to its micro-lens to coincidence between images of all fibers formed by the micro-lenses. After alignment, the lenslets and ferrules are potted by transparent epoxy to form a solid module. The ferrules with fibers are slightly tilted, so that the source at the center is well within their acceptance cone (numerical aperture) which, together with the lenslet size, define the field of view, $1\rlap{.}''5$ per quadrant. The four fibers terminate by the FC connectors plugged into the module of four photon-counting avalanche photo-diodes (APDs), model SPCM-A Q4C from Perkin Elmer. The measured optical transmission is 0.7. The acrylic lenslets do not transmit the UV light, so the probes are not affected by the LGS even without any protective filters.
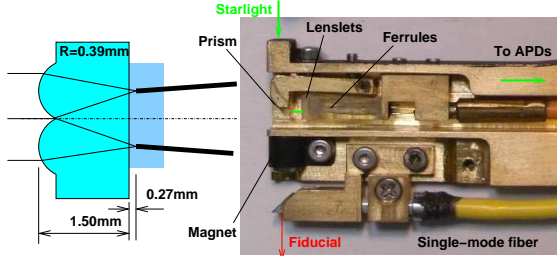
Figure 4. Optics of the SAM guide probe (left) and the actual device (right), with the light path in green overlaid.

The right-hand part of Figure 4 shows the actual guide probe without cover. The light from the telescope passes through a 3-mm hole and is deflected by a 3-mm right-angle prism before being focused on the lenslets and injected into the fibers. Tilts of the prism allow co-alignment of the optical axis with the direction of the incoming light, i.e. with the SOAR pupil. The back side of the probe facing SAM can project a point source created by a single-mode fiber and a red laser diode. This fiducial source is approximately coincident with the star. It proved very useful for a number of tasks, such as mapping the guide-probe coordinates on the CCD (to ease guide-star acquisition) and testing the optics of the AOM internally.

The APDs are cooled thermoelectrically within their modules to reduce the dark count which varies from 200 to 1500 Hz, depending on the detector. The high voltage (HV) enabling the avalanche amplification is turned on only after positioning the probes. To protect the APDs

from damage by over-light, we installed a circuit that switches off the HV as soon as the current exceeds some threshold. This hardware protection has saved the APDs when a room light was turned on accidentally during SAM integration. Guide stars (GSs) brighter than $V \sim 11$ mag sometimes trigger the over-light protection.

Comparison of the V magnitudes of the GS with the actual counting rate shows a scatter of about 1 mag, mostly because of unreliable photometry in the USNO-2 catalog. The mean flux F (sum of counting rates in the four quadrants) follows the expected trend

$$F[\text{kel/s}] = 10^{0.4(V_0 - V)}, \qquad (1)$$

with the zero points V_0 of 19.9 and 19.7 mag for GP1 and GP2, respectively. These zero points match the estimated sensitivity. A star of $V = 18$ mag gives a flux of 5.75 kel/s (or 57 counts per 10 ms loop cycle) in GP1. A Gaussian star of $1''$ Full Width at Half Maximum, FWHM (rms width $0\rlap{.}''42$) will have a centroid error on the order of $0\rlap{.}''02$ in the 10-Hz servo bandwidth. We do guide on $V = 18$ mag stars when no better choice is left.

The $3''$ aperture of the GPs is smaller than the pointing error of SOAR. To acquire a GS, we first take the pointing exposure with SAMI and determine the offset by measuring position of a star with known coordinates in the image. The GP is then positioned on the selected GS automatically, the HV on the APDs is turned on. If the star is detected, the GP can be centered on it manually; however, by closing the TT loop the star is centered automatically. Manual centering of at least one GP is required if both GPs are used, so that both GPs work near null. If the star is not detected, we use a software tool that modulates the tertiary mirror circularly with increasing radii of $1''$, $3''$, and $5''$. This effectively enlarges the capture zone of the GPs. If the modulated signal is detected, the GP is moved towards the star. Otherwise, we revise the pointing offset or select another star (some "stars" in the USNO-2 catalog are galaxies not suitable for guiding).

3.5. *Turbulence simulator*

The AOM contains a built-in artificial UV light source than can be injected in the optical path instead of the LGS. The focus and pupil of the simulated beam mimic the actual LGS; the beam can be artificially distorted, simulating the turbulence. This device, called TurSim, is essential for the SAM operation; it is used for flattening the DM and testing the health of the AO loop during daytime.

The 365-nm UV light in TurSim is emitted by the photo-diode from Nicia, with a diffuser and a circular aperture to emulate a $1''$ star. Two DC motors with cam mechanisms translate the source laterally and serve for centering its image in the WFS. The beam is collimated by a custom UV triplet lens, passes through the pupil mask simulating central obscuration, and is re-imaged by another lens group with the telescope's focal ratio, at a fixed axial position corresponding to the LGS at 7 km. One or two phase screens can be inserted in the parallel beam near the pupil mask to simulate turbulence of variable strength and speed; they are driven by regulated DC motors. The phase screens, made in-house (Thomas 2004), do not match exactly the expected Kolmogorov

spectrum, but this is not critical for testing SAM. Tur-Sim has a deployable arm for projecting the simulated LGS on-axis. With a total of seven mechanisms, it is a rather complex subsystem. To transmit the TurSim light through the WFS, its Pockels cell is triggered by internally generated pulses rather than by the laser.

3.6. AOM structure and mechanisms
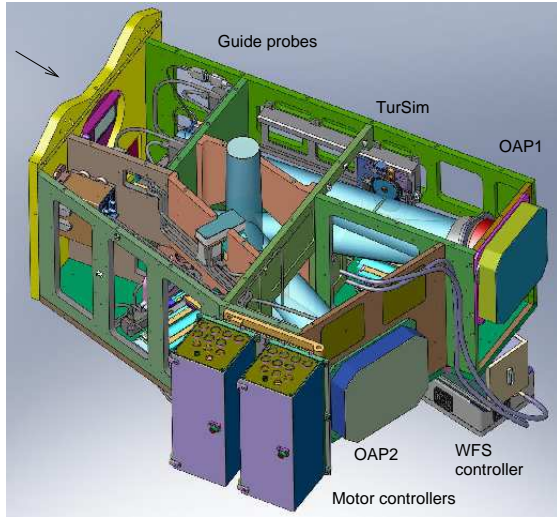
Figure 5. Mechanical structure of SAM.

All elements of SAM are housed in a box-like aluminum structure, called bench (Figure 5). It provides stiffness against gravity change in one direction as SAM rotates at the Nasmyth focus. The total range of flexure, measured by displacement of the image of the light source in the GP on the science CCD, is only $\pm 0''\!.35$. To prevent image blurring by flexure, avoid long exposures near the zenith associated with large rotation during the exposure.

The SAM bench is made of aluminum plates bolted together. They have large rectangular openings to access the optics and mechanisms of SAM. The covers are hermetized to prevent light and dust from entering SAM. For the same reason, the entrance opening of SAM is covered by an environmental shutter, opened only during observations.

The total mass of SAM (including SAMI) is 330 kg. An instrument up to 70 kg can be mounted on the visitor port. The mechanical design of SAM was complicated because of the space restrictions at the Nasmyth focus.

The AOM has 23 remotely controlled motions (e.g. 6 in the guiders, 7 in TurSim, 3 in the ADC, etc.). To reduce heat dissipation inside the instrument, all motor controllers are housed in two glycol-cooled boxes attached outside the bench. However, the APD modules and the driver of the Pockels cell are located inside SAM, as well as the WFS detectors CCD-39 and GC650.

3.7. SAMI, the CCD imager

The CCD imager, SAMI (Table 2), uses the 4096×4112 CCD231-84 detector with a pixel size of 15 μm manufactured by e2v. The chip has an astro broad-band anti-reflection coating providing a quantum efficiency of up to 0.90. It has an excellent cosmetic quality without any

Table 2
Parameters of SAMI

Parameter	Value
Format H×V (pixels)	4096×4112
Pixel size (arcsec)	0.0455
Field of view (arcmin)	3.07
Gain (el/ADU)	2.1
Readout noise (electrons)	3.8
Zero point in SDSS g' & i' (mag)	24.4 & 24.7

major blemishes. The CCD is read out through four amplifiers using the SDSU-III controller, as in the WFS. The full frame without binning is read out in about 8 s, with a readout noise of 3.8 electrons and a gain of 2.1 electrons per ADU. Most of the time, the imager uses a 2×2 binning, or an effective pixel scale of 91 mas. The CCD is housed in a dewar cooled by liquid nitrogen and maintained at stabilized working temperature of $-120°$C. A blade shutter in front of the CCD allows exposure time as short as 0.1 s, although longer exposures are recommended to ensure good photometric uniformity. The filter wheel is mounted before the shutter.

The SAMI software provides a standard functionality: acquisition of single or multiple images of the full frame or of a region of interest. The image headers contain information received from the telescope, as well as the state of the SAM instrument. The SAMI software can be driven externally, e.g. by a script that synchronizes exposures with stepping of the Fabry-Perot etalon inside SAM. Dithering can be done by a script in the SAM software. However, recombination of images taken with large dithers requires prior correction of their distortion.

The photometric zero point of SAMI in the SDSS g' band (stellar magnitude of a source giving a flux of 1 ADU/s) is 24.4 mag (Tokovinin 2014). This corresponds to the overall quantum efficiency of 0.46, which is quite high considering light losses in the atmosphere, telescope, SAM optics, and filter. The response of SAMI is higher than that of SOI, a simple optical imager at SOAR with a focal reducer in front of the CCD.

4. LASER SYSTEM

The LGS is produced by Rayleigh and aerosol (Mie) scattering of light at 355 nm wavelength from the pulsed laser, projected on the sky through a small telescope, LLT. Main optical elements of the laser system are listed in Table 3 (CC stands for conic constant).

Table 3
Optical elements of the SAM LGS

Element	Description
Laser	Tripled Nd:YAG, 10W, 355 nm
Beam expander	8x magnification
LGS M4 mirror	$D = 25$ mm
LLT fold mirror	UV mirror
Phase plate	UV $\lambda/4$
LLT M2 mirror	Spherical $D = 15$ mm, $R = 30$ mm
LLT M1 mirror	$D = 250$ mm, $R = 840$ mm, CC=-0.967

4.1. The UV laser

The laser (model Q301-HD from JDSU) is a frequency-tripled pulsed Nd:YAG with a nominal average power of

10 W. It is located on the telescope truss, in a thermal box maintained at $+20°C$ temperature and flushed with dry air. In the real operation (under variable gravity and at the altitude of Cerro Pachón) the internal power meter of the laser indicates its output power in the range from 7.5 W to 7.8 W. The beam quality measured in the laboratory is very good, $M^2 = 1.05$. We operate the laser at its nominal pulse frequency of 10 kHz. The pulse duration is about 34 ns. The JDSU company fabricated hundreds of such lasers, mostly for photo-lithography, so it is a rugged industrial product. So far, we had no problems with the laser; it works without any servicing, apart from the coolant refreshment every year or so.

4.2. *Beam transfer optics*

The narrow beam emerging from the laser is expanded to the diameter of $\sim$8 mm (at $1/e^2$ intensity level) and directed to the LLT with one reflection from the LGS-M4 mirror at the SOAR top ring. The beam path to the LLT is enclosed in a 1-inch aluminum tube for safety and dust protection. The decision to expand the beam was taken to reduce its intensity on the path to the LLT (less coating damage and more tolerant to dust on the optics) and to have extra flexibility for adjusting the diameter. The laser box has a fast safety shutter. During alignment, a mirror can be inserted in the light path to substitute the UV beam with a green laser pointer.

Tilts of the LGS-M4 mirror are controlled remotely for centering the beam on the LLT. Four UV photo-diodes around the LLT primary mirror and the 5th diode on-axis serve for the beam diagnostic. The tilts of the LGS-M4 are regulated to center the beam by balancing the four photo-diode signals approximately, while the laser beam is propagated in the dome during daytime. Signals of these photo-diodes serve as a useful diagnostic of normal LGS operation.

The size of the beam on the LLT mirror is adjusted by the magnification and/or focus of the beam expander in the laser box. It is measured by the signal ratio of the peripheral and central photo-diodes and/or by the shape of the UV beam at the LLT exit, visualized by luminescence of a standard white paper and photographed (this beam is not very intense, hence safe). The beam on the LLT mirror has FWHM diameter of 125 mm.

4.3. *Laser Launch Telescope (LLT)*

The design of the LLT (Figure 6) is constrained by the small space available behind the SOAR M2. Its 25-cm aperture was chosen to minimize the LGS spot size, balancing between the diffraction and the atmospheric blur. For sodium lasers, the LLTs have typical diameters of $\sim$0.5 m, but for the UV the optimum LLT diameter is reduced in proportion to the wavelength. In hindsight, the SAM LLT could be even smaller because in reality the atmospheric blur of the LGS dominates over diffraction.

The LLT optics consists of the spherical secondary mirror M2 and the fast elliptical primary M1 (a Dall-Kirkham telescope). Spherical M2 is easier in fabrication and alignment, but such optics has only a small FoV, limited by the off-axis coma aberration. Although the LGS beam is on-axis, the FoV of $\sim 1'$ is needed for co-alignment between LLT and SOAR, compensating the flexure of both telescopes. This requirement is fulfilled
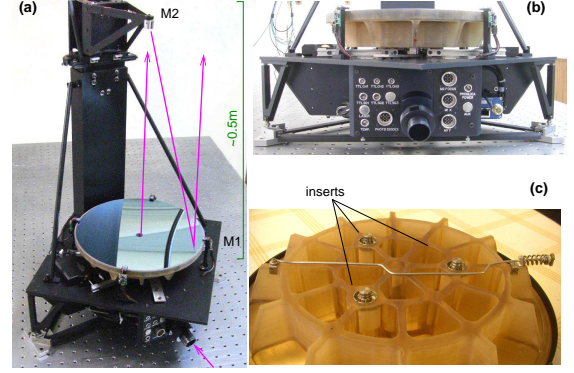
Figure 6. The LLT. Photo on the left (a) shows the LLT without enclosure, with the laser light path depicted in pink. The photo (b) is a side view from the input panel with connectors, showing how the primary mirror is suspended on the flexures. In (c) the back side of the light-weighted primary mirror is shown. The mirror diameter is 25 cm.

by mounting the M1 on three flexure rods that point to its focus. Lateral motions of M1 are thus converted into its rotations around the focal point. As M1 is actuated to steer the LLT beam on the sky, it stays perpendicular to the beam, thus avoiding the off-axis coma. The flexures also serve as a kinematic M1 mount.

The LLT M1 was fabricated by S. Potanin using a 5-cm thick Astro-Sitall (Zerodur analogue) blank, light-weighted by removing most of the material from the back side and leaving the rib structure. Three Invar inserts are glued into the circular pucks machined in the blank to connect mirror with the flexures. Although the thermal expansion coefficients of Zerodur and Invar are both about 10^{-7}, the 0.1-mm layer of the epoxy glue around the inserts produced thermal deformation of M1. The problem was fixed by replacing the solid inserts with flexible equivalents that do not stress M1.

The M2 mirror is mounted above M1 on a column, attached to it by a light-weight truss and flexures. This allows its axial motion for focusing. The distance between M1 and M2 is fixed by an Invar rod, actuated for focusing by a motor near M1. In this way, the LLT focus is not very sensitive to temperature changes, despite its aluminum structure. Lateral position of M1 is defined by two motors that act on its flexures laterally, in a kinematic arrangement. The LLT internal structure is very stiff and light-weight. It is connected to SOAR via three mounting points. The box-shaped LLT enclosure is attached to the same points independently of the main opto-mechanical assembly. The environmental shutter of the enclosure is a thin steel sheet that slides to the side when opened.

The 8-mm parallel beam arriving at the LLT after reflection from the LGS-M4 is deflected towards LGS-M2 by the tertiary mirror LGS-M3, mounted on the piezo-electric tip-tilt platform (S-330 from Physik Instrumente) for fast beam steering. The platform is driven by the average spot centroids in the SAM WFS and keeps the spots centered in the WFS in closed loop. Remember that the SOAR M3 is actuated in TT to stabilize the science image; this also displaces the LGS, so the LLT TT servo has to compensate for this disturbance and for the intrinsic beam wander of the LLT itself, to keep the spots centered. The range of the LLT fast tilt servo is $\pm14''$ on one axis and $\pm10''$ on the other axis, reduced

by oblique reflection from the LGS-M3. The LGS can be steered over a larger range by the M1 lateral actuators, while the piezo platform compensates only small and fast residual tilts.

The LGS-M3 with a dielectric UV coating is almost transparent to the visible light. Below it, a small "telescope" is located to capture the collimated light of a bright star, for co-alignment between LLT and SOAR and for testing the LLT image quality. It uses the GC650 CCD camera, as in the WFS acquisition channel. This device can also back-project a parallel beam from a red laser diode through the LLT. We mount a 20-cm flat mirror in front of the LLT to reflect the emerging red beam back, and test the LLT optics in auto-collimation. This functionality proved critical for *in situ* testing and alignment of the LLT. On 2015 September 16, the strong earthquake caused an acceleration up to ∼5g at the SOAR M2. The LLT was slightly misaligned, but could be re-aligned quickly by tilting the spherical M2, using the auto-collimation mirror and the red diode beam.

The size of the LGS spots in the WFS often exceeded $2''$, well above the expected seeing blur. Partly it was caused by the heat dissipated by the LLT electronics located just beneath it. The electronics was modified and is now powered only when the LLT motors are actually used. As a result, the LGS spots became smaller. However, they are still enlarged sporadically by internal seeing in the SOAR dome.

The $\lambda/4$ wave plate located above the LGS-M3 transforms elliptical polarization of the laser beam into circular polarization propagated in the sky. There were several incidents when insects, attracted by the UV light, got inside the LLT and were burned, damaging either the $\lambda/4$ plate or the window of the laser box. These elements were easily replaced, without need for realignment. To prevent further damage, we covered the LLT aperture with a metallic mesh (3-mm pitch and 0.1-mm thickness). It causes only a minor light loss of ∼12% through blocking and diffraction.

5. COMPUTERS AND SOFTWARE

5.1. *Real-time computer and software*

The SAM real-time computer (RTC) is a standard PC with an Intel[R] Core Duo processor E7500 running at 2.93 GHz. It works under CentOS release 5.8 operational system (Linux kernel version 2.6.25 #5 SMP) with a real-time patch RTAI 3.8. The RTC is located in the SOAR computer room. It contains the acquisition board of the SDSU CCD controller receiving the WFS signal and the waveform generator board for the M3 control. Other interface modules of the RTC are housed in the PXI chassis in the SAM electronic rack. The fiber connection between RTC and PXI effectively brings the computer bus towards the instrument. The PXI chassis must be powered when the RTC is booted. The PXI contains two 32-channel digital-to-analog converters that generate the DM drive signals and the timer/counter boards for acquisition of counts from the TT APD detectors. Another timing board generates the range-gate pulses of programmable delay and duration.

The *real-time core* (RTCORE) is at the heart of the AO control. Each control loop cycle is triggered by an interrupt from the acquisition board when the fresh CCD frame arrives. The spot centroids are computed using a standard center-of-gravity algorithm. Several alternative centroid algorithms such as correlation or weighted centroid (Thomas et al. 2006) are available and have been tested, but we found that with the 2×2 binning and the small WFS aperture the standard centroid gives the smallest noise.

The wave-front slopes are the differences between the current centroids and the reference spot positions. The 144 slopes from 72 sub-apertures are multiplied by the 60×144 reconstructor matrix, and the resulting 60 DM drive voltages are filtered temporarily by the loop controller (integrator with a gain of 0.25). The reconstructor matrix typically contains 38 to 40 system modes (weak modes are rejected in the reconstructor calculation). To prevent growth of unseen modes, a leak of 0.01 is introduced. A somewhat faster second-order temporal controller (so-called Smith predictor) is implemented, but it gives no sizable improvement over the simple integrator.

When using the LGS, the standard AO control scheme is modified. Slopes averaged over all subapertures are subtracted from the high-order control signals. Those average slopes instead are driving the tip-tilt platform in the LLT to keep the spots centered in the WFS. The two control voltages for the LLT are generated together with the 60 DM voltages.

Occasionally, the LGS spots become blurred or contain too few photons because of clouds. Some spot centroids then remain indeterminate. Those "missing slopes" do not participate in the calculation of the average tilt and are replaced by zeros in the high-order loop control. The AO loop is robust against subapertures with missing information.

The RTCORE communicates with the non-real-time applications written mostly in LabView. They include the graphic user interface (GUI) and various service modules. A bank of shared memory containing slopes and DM voltages is used for the analysis of the AO loop performance (e.g. temporal power spectra of Zernike modes), estimation of atmospheric parameters and residual aberrations. Some of those diagnostic data are saved in the log file and in the image headers. Samples of AO data (slopes, DM voltages, TT signals, and WFS frames) can be saved by the SAM operator for further off-line analysis and archiving.

5.2. *Instrument control*

Apart from the real-time software, the SAM instrument is controlled by four other software modules running in the instrument computer (IC), also operated under Linux. The IC is housed in a cabinet on the SOAR mount platform. All instrument control software is written in LabView; each module has its own GUI. The software is accessed by VNC connections either from the SOAR control room or remotely.

Two modules (one for AOM and one for LGS) take care of the motion control and other hardware. The motor controllers, switches, and telemetry boards of the AOM are all connected to the serial RS-485 line acting as a bus and accessed by a communication board in the IC. The laser subsystems are controlled in a similar way, with an addition of the direct serial communication with the laser.

Each controlled motion (e.g. the WFS focusing stage)

has to be initialized (search for the zero-point mark) after powering the instrument. Then the controllers "know" the current mechanism positions and can move them using incremental encoders. To speed up the start-up process and to avoid unnecessary motions, all current mechanism positions are saved by the software and re-loaded in the controllers at the start, thus by-passing the initialization. This is particularly important for the LLT mechanisms that are powered only when actually used and hence must "wake up" quickly. The exception is made for the guiders: their six motors are initialized after each power-up. This is done to avoid the risk of collision between the GPs (their trajectories can overlap). Collision is avoided by the motion control software, while an additional hardware anti-collision sensor is implemented as an extra precaution.

The instrument control software (ICSOFT) of SAM is a high-level LabView application used to operate the whole instrument. It communicates with the lower-level modules (motion control and RTSOFT) and the telescope through sockets. In normal use, SAM is controlled only through the ICSOFT GUI and there is no need to access other modules. ICSOFT has a scripting capability to code sequences of actions, thus simplifying SAM operation. For example, search for guide stars by the SOAR M3 modulation with increasing amplitude, their detection and re-positioning of GP when the star is found is done by a script activated by a single button. There are scripts for preparing SAM for observations and shutting it down at the end of the night. A software tool for visualization of the WFS acquisition images and a star catalog software for selecting guide stars are run together with the ICSOFT during SAM operation.

5.3. *Laser safety*

SAM operation is subject to restrictions on laser propagation imposed by the US Space Command and managed by the Laser Clearing House (LCH). Lists of target coordinates are sent to the LCH several days prior to the observations, and the authorized laser propagation windows for each target are received on the day of operation, or a day before. These files are loaded in the software module that automatically shutters the laser when the telescope coordinates differ from the target coordinates by more than $120''$ or when the propagation is not authorized. This software receives information from the telescope control system. Both the internal laser shutter and the fast safety shutter in the laser box are closed. Typical LCH interrupts last a few tens of seconds, while their frequency varies from a few per hour to one or none per night, depending on the target location. Blanket laser closures occasionally announced by the LCH are introduced manually in the software and then enacted automatically.

The SAM laser does not present any hazards to the airplanes. Its UV radiation is not visible and does not penetrate the eye, being absorbed by the cornea. As a result, the safe illumination level is much higher compared to the visible-light lasers. An airplane going through the SAM beam receives only one laser pulse, as the next pulse falls at a different non-overlapping location; the resulting illumination is 100 times less than the safe threshold for eye and skin established by the US safety standard ANSI Z136.6-200.

The narrow beam of the SAM laser and even the expanded 8-mm beam are hazardous to people. Work with those beams involves standard laser safety precautions and can be done only be qualified personnel. In normal operation these beams are encapsulated inside boxes and beam conduits. The beam emerging from the LLT is sufficiently diluted to be safe; moreover, it is not accessible from anywhere inside the dome. Consequently, the SAM laser in normal operation does not require any safety measures. Nevertheless, a luminous sign in the telescope control room warns when the laser diodes are energized. A safety circuit and several emergency stop buttons are implemented to shut down the laser in abnormal situations.

6. PERFORMANCE OF SAM

#### 6.1. *Requirements and error budget*

The basic requirements follow from the intended use of SAM: (i) provide a non-negligible improvement of the image resolution, with a FWHM of 2/3 compared to the uncorrected seeing, (ii) FWHM variation of $< 10\%$ over the field, and (iii) sky coverage of no less than 90%. The remaining requirements relate to the instrument use (e.g. one-person operation), operating conditions such as temperature range, etc. A large number of technical requirements were formulated to guide the instrument design.

The quality of AO compensation is normally characterized by the Strehl ratio, which translates to the residual wavefront error. In GLAO the goal is to reduce the PSF size, so the Strehl ratio is not an adequate metric. The expected performance of SAM was first evaluated for an ideal instrument, considering the finite compensation order, the geometry of the LGS, and the turbulence profiles measured at Cerro Pachón (Tokovinin & Travouillon 2006). The PSF is computed from the structure function of residual wavefront errors (RSF) which, for SAM, grows almost linearly with the distance. The corresponding PSF has a sharper peak and stronger "wings" compared to the seeing profile; it can be well approximated by a Moffat function with $\beta = 1.5$ (Tokovinin 2008, see equation 1 below).

In the real instrument, the errors of the spot centroids, TT residuals, and servo lag degrade the performance somewhat. The combined errors of the SAM AO were required not to degrade the ideal resolution by more than 10%, meaning that their relative contribution to the RSF at the characteristic baseline of 0.5 m should not exceed 10%. In this way, the error budget and requirements to various AO subsystems were developed (Tokovinin 2008). Unlike the standard Strehl-based approach to the AO design, it constrains only the difference between the real and "perfect" SAM and does not depend on the fixed instrument parameteres and turbulence profile.

6.2. *Performance of the AO loop*

When SAM was first installed at SOAR in 2009, we found that the axis of the Nasmyth rotator did not point to the center of the pupil. As a result, rotation displaced the pupil image on the LLA. This has been adjusted by tuning the angle of the SOAR M3, so that rotation-induced pupil motion became less than 0.2 of the sub-aperture size. The diameter of the pupil image on the LLA was measured by recording sky through the WFS,
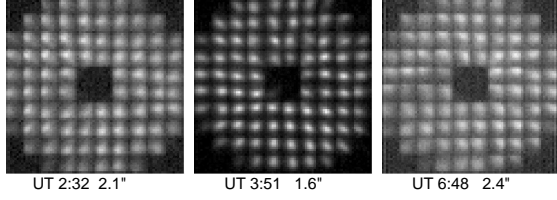
Figure 7. LGS spots in the SAM WFS in the 2013 September run, illustrating the spot size variation from 1″6 to 2″4, depending on the seeing.

measuring flux in each sub-aperture, and fitting a model with three parameters: pupil diameter and its lateral shifts. The optimum pupil radius is 5.1 sub-apertures, the actually measured one is 4.8 sub-apertures. This causes a loss of flux in the peripheral sub-apertures and a mismatch between the interaction matrix measured with TurSim and the actual LGS.

With a typical range gate of 0.15 km (maximum spot elongation of 1″25) and the loop frequency of 478 Hz the return LGS flux varies between 200 and 800 electrons per sub-aperture per loop cycle. The flux depends on the spot size (large spots are truncated by the WFS aperture), atmospheric conditions (more photons are scattered by aerosols or less photons due to additional absorption by thin clouds) and the rotator angle (the polarization adjustment in the WFS is not perfect). Light losses in the up-link and down-link LGS path lead to the estimated (and measured) total efficiency of 5%. This number, combined with the lidar equation, implies the return flux of 600 photons per sub-aperture per loop cycle, as actually observed under favorable circumstances.

The FWHM size of the LGS spots is measured by stacking many WFS frames and fitting Gaussians to several spots around the pupil center (the elongation due to the finite range gate is thus small). It ranges from 1″3 to 2″3, depending mostly on the local seeing (Figure 7). The rms centroid noise is normally between 0.15 and 0.25 pixels. Figure 8 gives an example of the AO loop performance on a night with mediocre atmospheric conditions.
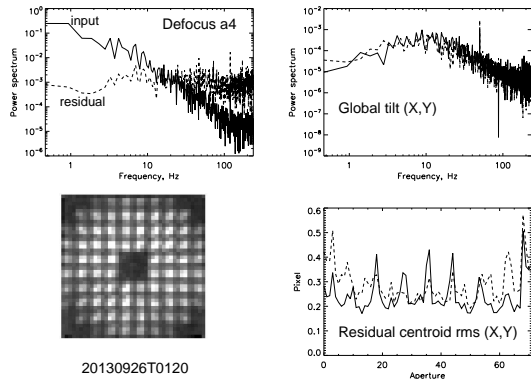
Figure 8. Performance of the SAM AO loop on 2013 September 26 at 1:20 UT. Top left: temporal spectrum of the Zernike defocus coefficient a_4 (residual in dashed line, input in full line, variance 1.2 rad^2). Top right: temporal spectra of the global tilt in the WFS in X (full line) and Y (dashed line), rms 0.35 pixels. Lower left: average WFS spots (flux 160 kel/s, spot size 1″61). Lower right: residual centroid variance in each sub-aperture (X in full line, Y in dashed line) in WFS pixels, with the global tilt subtracted.

The TT loop uses signals of one or two GPs to control the angles of SOAR M3. The temporal controller accounts for the frequency response of M3, which eventually restricts the TT bandwidth to ∼10 Hz. As the TT probes are quad-cells, the loop gain depends on the seeing. With a very good seeing and a gain too large, the 15-Hz oscillation appears, so the nominal TT gain is set to avoid such situations. The optical axis of SOAR vibrates with a frequency of 50 Hz and a typical rms amplitude between 20 and 50 mas. The cause of this vibration is not yet established, but it is clearly seen in the spectra of the TT signal. This vibration is too fast to be compensated by the TT loop. Fortunately, its contribution to the FWHM resolution is only marginal under normal use of SAM and long exposures. The 50-Hz vibration is a very serious factor in speckle interferometry, forcing to use exposures shorter than 10 ms and affecting the limiting magnitude.

### 6.3. Delivered image quality
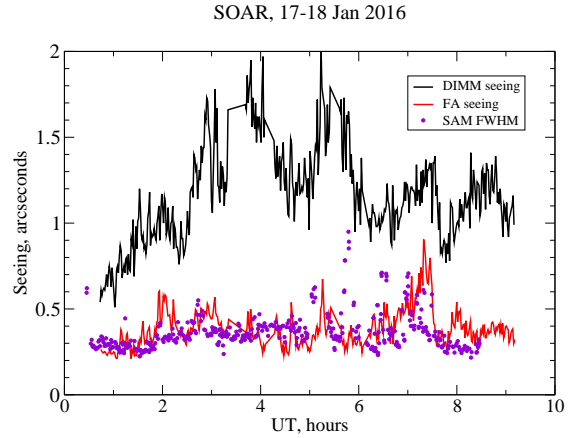
Figure 9. Atmospheric conditions and FWHM resolution of SAM on 2016 January 17. Series of short-exposure images were recorded with HRCam in the I band, co-added with re-centering, and approximated by a Moffat function. The outlying data points correspond to the data taken in open loop. The black and red curves correspond to the total and free-atmosphere (FA) seeing measured by the site monitor.

The gain over natural seeing brought by SAM is quantified by several metrics: by the FWHM resolution and its uniformity over the field, by the PSF profile and its variation, and by the increased energy concentration. The normalized rotationally-symmetric PSF $I(r)$ is frequently approximated by the Moffat function

$$I(r) = [1 + (ar)^2]^{-\beta} \qquad (2)$$

with two parameters a and β; the FWHM is $(2\sqrt{2^{1/\beta} - 1})/a$. The case $\beta = 1$ corresponds to the Lorentz profile, whereas the seeing profile under Kolmogorov turbulence is well modeled by $\beta \approx 4.77$.

The SAM PSF under good compensation corresponds to $\beta \approx 1.5$, in agreement with its predicted shape (see § 6.1 above). Compared to the seeing-limited PSF, it has a sharper core and stronger wings. The gain of SAM depends on the metrics used and cannot be expressed by a single number. Here we quantify it by the FWHM
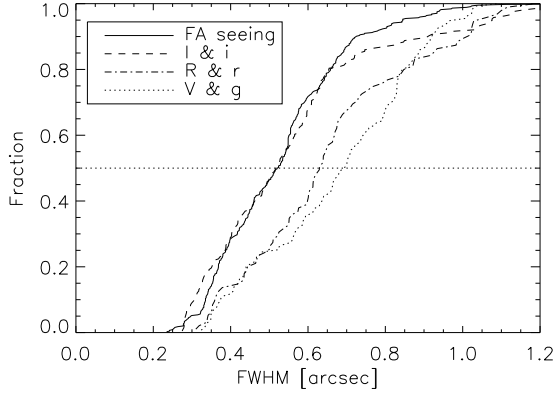
Figure 10. Cumulative histograms of the free-atmosphere seeing (full line) and SAM FWHM in various filters for eight nights in January, February, and September 2013. The medians are 0.″52 for both the FA seeing and the FWHM in the I or Sloan i' bands, while the median FWHM in R or r' is 0.″63 and the median FWHM in V or g' is 0.″70.

resolution. If SAM improves it by a factor of 2, the gain in the central PSF intensity is about 2.8 times, while the half-energy diameter is reduced only by ∼1.5 times compared to the seeing.

The FWHM resolution at long wavelengths (e.g. in the I band) closely follows the free-atmosphere (FA) seeing measured by the MASS instrument (Figure 9). According to Tokovinin & Travouillon (2006), the median FA seeing at Cerro Pachón is 0.″40. At shorter wavelengths, the gain in resolution over seeing is less because the compensation order of SAM is not high enough. Still, the resolution gain in the R and V bands remains substantial. However, when the total seeing is dominated by the high-altitude turbulence, SAM brings no improvement because it does not sense this high turbulence. Turbulence sensing by SAM decreases with distance progressively and turbulence at, say, 0.5 km is compensated to some extent, but the compensation is always partial because of the finite AO order, servo lag, and noise. So, the resulting SAM performance depends on a number of factors. However, the simplistic rule of thumb that SAM resolution is almost always close to the FA seeing turned out to be remarkably good in practice, as demonstrated by plots similar to Figure 9 that appear in (Tokovinin 2013, 2014).

Figure 10 shows cumulative distributions of the FWHM in several filters in eight nights during three SAM runs in 2013, under a variety of turbulence conditions. Each point is a median FWHM of all stellar sources in one closed-loop exposure, not corrected to zenith. The histogram of the FA sesing at zenith measured by MASS, matched in time to the SAM exposures, is plotted for comparison. The FWHM in the I or i' filters (214 estimates) equals the FA seeing in ∼80% of the exposures, with the same median of 0.″52. The remaining 20% are affected by very poor total seeing and, for deep exposures, by semi-resolved distant galaxies which bias the median FWHM estimates to larger values. On the other hand, the 53 exposures in Hα taken under a median FA seeing of 0.″32 have a median FWHM of 0.″35.

The uniformity of correction over the 3′ field depends on the atmospheric conditions. Both the uncorrected high turbulence and the well-corrected ground layer do not cause PSF variation in the field, but the partially

corrected turbulence in the "gray zone" (at a few hundred meters) leads to the non-uniformity, with a better resolution on-axis (Tokovinin 2004). This phenomenon is actually observed,[2] but in general the FWHM is very uniform over the field and rarely degrades by more than a few percent towards the edge (Figure 11). For the I-band data presented in Figure 10, we modeled the FWHM dependence on the distance from the CCD center by a linear function and found that the median linear coefficient is zero, within errors. The uniformity becomes even better at shorter wavelengths where the resolution gain becomes smaller. In principle, the resolution should depend on the distance from the TT star(s), but this effect has not been studied on the real data.

7. SCIENCE OPERATION OF SAM

SAM has been fully commissioned by the end of 2013. Some scientific results have already been obtained by that time using commissioning data (Fraga et al. 2013). Since the 2013B semester, SAM was offered in a shared-risk mode, and its science verification (SV) program was executed in 2014. Regular observing proposals for SAM are accepted since the 2014B semester. Like other SOAR instruments, SAM can be operated remotely from La Serena or from other location with a fast enough network connection.

7.1. *Operational sequence*

SAM is scheduled classically for specific nights, preferably grouped in runs (the instrument is switched off between the runs but stays on the telescope). Before each run, the SAM scientist starts the software and makes daytime tests following the standard checklist. This procedure has been successful in detecting hardware or software problems, leaving time for their fixes. For example, failures of the line transformer in the high-voltage DM driver, failed motor-control boards, or a stuck motor shaft. When possible, SAM is tested during engineering nights a few days before the science runs. Fortunately, we have not yet lost any significant night time to SAM failures.

The filters in SAMI are installed by the telescope operators during daytime, as in other SOAR instruments. SAMI can use either 4×4 inch square filters in a wheel with 5 positions or 3×3 inch filters in another 7-slot wheel. The limited number of filters restricts sometimes the number of science programs that can be executed with SAMI on any given night.

The overhead time, from the start of the telescope slew on a new target to closing all four loops, can be as short as 5 minutes, with 7 minutes being typical. Most of this time is spent for acquisition of guide stars. Owing to the small 3″ field of the GPs, the exact telescope pointing is determined by pre-imaging with SAMI; a star with known coordinates must be identified in this image to compute the pointing offset. *All* science targets observed so far had guide stars down to the $R = 18$ limit, i.e. the SAM has a complete sky coverage. Such a star gives ∼60 counts per 10-ms cycle of the TT loop.

---

[2] See Figure 21 in the SAM Commissioning Report, http://www.ctio.noao.edu/soar/sites/default/files/SAM/archive/samrep.pdf.
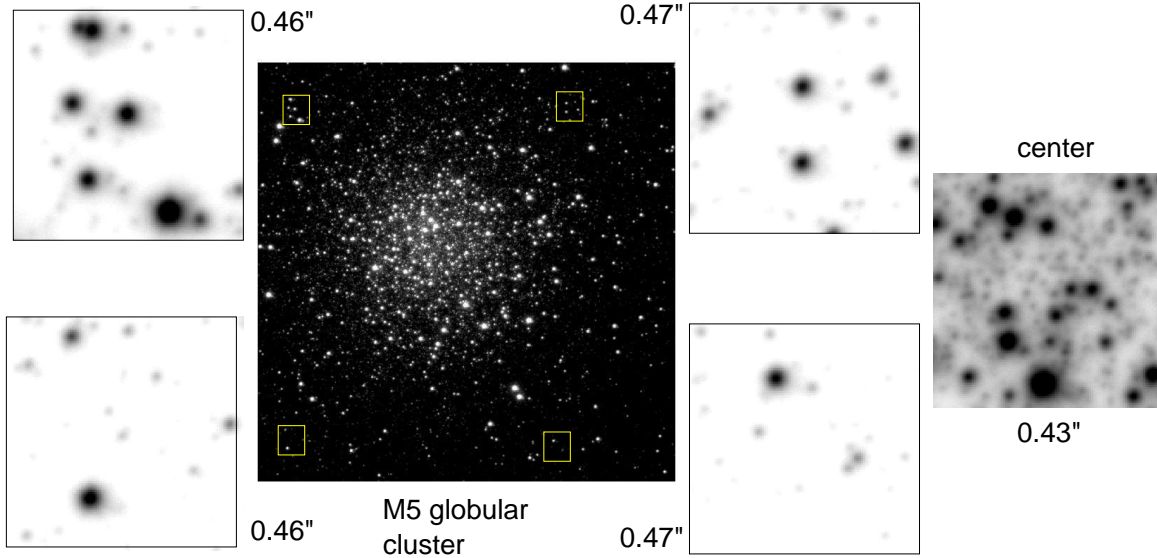
Figure 11. Image of the M5 globular cluster taken on 2013 March 2 (six 10-s exposures in the I filter, median-combined). The square fragments of $12''$ size in the corners and in the center of the image demonstrate the stability of the PSF over the entire field (the FWHM measured on several stars in each fragment is indicated).

The SAM *observing tool* (OT) is a custom IDL software that helps formatting the target lists for the LCH, but also allows pre-selection of guide stars and loading DSS2 images in the 5×5 arcmin field to assist in field identification. Guide stars pre-selected in the OT can be fed to the SAM software and used alongside with the catalogs.

When the TT loop is closed, the SAM operator opens the laser shutter and acquires the LGS. For LGS centering, the un-gated LGS image is captured by the WFS acquisition camera. The LLT electronics is powered on and the LGS is centered, compensating for differential flexure between the LLT and SOAR optical axes (typically less than $10''$). Then the LGS tilt loop is closed, and the high-order loop is closed as well (the LLT electronics is powered off automatically at this time by the script). The LGS acquisition is straightforward and takes less than a minute. If the telescope slew was small, the laser photons reach the WFS without re-centering the LLT, in which case the two LGS loops are closed within a few seconds. Experience shows that SAM often remains operational with a light cirrus clouds because the LGS is located below the clouds.

Time remaining until the next LCH interrupt is displayed in the ICSOFT. A few seconds before the interrupt, the LGS loops are opened automatically, while the science exposure is normally paused by the observer. The SAM operator closes the laser loops manually after the interrupt.

The first target of the night is usually used to check the relative focus between SAM WFS and SAMI. The focus might change because of temperature or because of SAMI filters of non-standard thickness, although it was found to be quite stable. To test the focus, two short exposures are taken with closed AO loop and WFS defocused by ± 4 mm from the nominal. The SAM PSF should be enlarged by the same amount if the nominal focus is correct. Otherwise, the correct focus setting of the WFS stage is found by linear interpolation between bracketing exposures.

SAM can operate in open loop, without laser. In such case, the DM is flattened passively. The LGS, if available, still helps to focus the telescope in open loop by measuring the focus term and nulling it by adjusting the telescope focus. Open-loop operation happens when the image quality is not critical or for targets that are not in the LCH list (e.g. photometric standards).

### 7.2. *Projects done with SAM*

During 2014, SAM received only a small number of proposals, but its use has steadily increased in 2015, making it the second most popular instrument at SOAR.

By concentrating the light of stars in a smaller number of pixels, SAM reduces photometric errors in dense stellar fields dominated by confusion (Olsen et al. 2003). The gain in sensitivity in such case is proportional to the central intensity of the PSF.

The first science paper produced by SAM presented the color-magnitude diagram of the globular cluster NGC 6496 (Fraga et al. 2013). The FWHM resolution in these early commissioning data of 2012 May was excellent, reaching $0''\!.25$ in the I band. However, it was not uniform over the field, showing an asymmetry likely related to the wind direction (the SAM loop worked then with a low frequency of 233 Hz). Despite this, accurate photometry was possible by fitting field-dependent PSF with DAOPHOT. Presently, J. Santos (Brazil) is conducting a large survey of globular clusters in the Magellanic Clouds, exploiting the potential of SAM in crowded fields; eight nights in the 2015B semester were used successfully. Salinas et al. (2016) discovered new variable stars in globular clusters with SAM.

SAM can help in resolving close binary stars, especially the faint ones beyond the reach of speckle interferometry. The survey of faint low-mass companions to nearby stars has revealed one new $0''\!.2$ binary (Tokovinin 2014). However, for binary stars the "detection power" of SAM in terms of resolution and dynamic range is inferior to the classical AO in the infrared or to speckle interferometry.

Combination of speckle interferometry with laser-

SDSS   HST   SAM
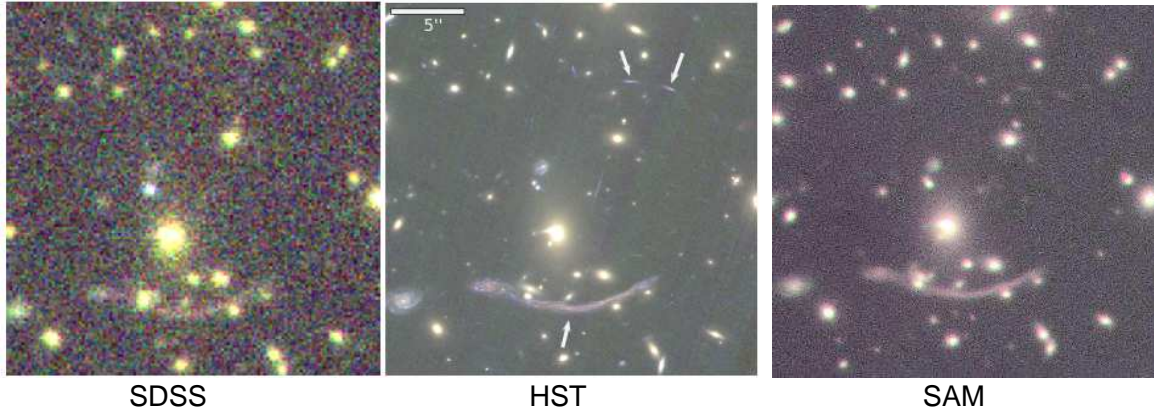
Figure 12. Images of the gravitational arcs in the galaxy cluster Abel 370 from SDSS, HST, and SAM. The SAM images were taken on 2013 September 29, 2013. Five 5-minute exposures in the SDSS i' and r' filters each are median-combined and presented as a false-color image with a FWHM resolution of $0\rlap{.}''5$.

enhanced seeing is a promising technique. It was used in 2015 May for the survey of *Kepler-2* field (Schmitt et al. 2016). SAM worked with the laser, but without guiding. Series of short-exposure images were re-centered and combined offline; the median FWHM resolution of the re-centered images was $0\rlap{.}''43$. Binarity of targets as faint as $I = 15$ mag could be probed down to $0\rlap{.}''15$ separation by the speckle image processing. This technique was used again in 2016 January to discover young low-mass binaries in Orion, in a project led by C. Briceño. The FA seeing was better than in May and the FWHM resolution of re-centered images reached $0\rlap{.}''25$ (Figure 9).

Several programs on emission-line objects are planned using SAMI with narrow-band filters. The Herbig-Haro jet HH 46/47 in the S[II] narrow-band filter was observed with SAM on 2015 February 14, yielding a FWHM resolution of $0\rlap{.}''45$. Continued observations with SAM use a combination of custom narrow-band filters to probe physical conditions in the jets.

The team of A. Ardila observed with SAM nearby galaxies NGC 1232 and NGC 1482 in the Hα band to study star-formation regions with high spatial resolution. The data are still being analyzed, while nice images resulting from this effort were generated with a resolution twice better than in the image of NGC 1232 from the VLT press release.

During three nights in 2015 SAM worked with a Fabry-Perot (F-P) etalon inserted in its collimated beam after the ADC, on a translation stage (Mendez de Oliveira et al. 2016). The existing F-P etalon with a spectral resolution of about 11 000 just fits in the available space, with 1-mm gaps on both sides. Selection of one F-P order is done by the interference filters in the SAMI wheel. This project is led by C. Mendez de Oliveira and P. Amram. To overcome the SAMI readout noise, the binning of $4{\times}4$ (pixels of $0\rlap{.}''18$) was used.

Some science verification programs intended to use SAM for detecting faint nebulae around stars. In this area, SAM has no advantage over other ground-based imagers; it concentrates the light in the core of the PSF but does not reduce its wings.

SAM is well suited for high-resolution imaging of faint deep-space objects. Here its complete sky coverage and a moderately wide $3'$ field play an essential role. D. Murphy used SAM in 2013 for two nights to get a very deep high-resolution image of a peculiar galaxy in a cluster,

apparently affected by recent interaction (Murphy 2015). Spectacular images of thin gravitational arcs produced by lensing distant galaxies were obtained with SAM during its commissioning (Figure 12). No proposals for continuing this effort have been accepted so far. However, the program by V. Motta was started in 2015 December and continues in 2016. Her team took high-resolution images of lensed quasar candidates revealed in a wide-field survey. This is an excellent example of the future use of SAM, where it will complement wide-angle surveys by studying interesting objects with higher spatial and/or spectral resolution.

Yet another promising application of SAM will be to study globular clusters (GCs) in other galaxies. Even a small gain in resolution over seeing might be critical here to distinguish GCs from stars. Results in this area are reported by Salinas et al. (2015).

8. SUMMARY AND OUTLOOK

The crucial role of the Hubble Space Telescope (HST) in astronomy, despite its moderate 2.4-m size, demonstrates the need of high angular resolution at optical wavelengths, so far not provided by ground-based AO instruments. The resolution delivered by SAM is still much inferior to the resolution of the HST, which continues to be the facility of choice. The advantages of SAM compared to the HST are its accessibility and the larger telescope aperture, hence the larger number of collected photons. When very faint objects are observed in narrow spectral bands, the minimum size of the resolution element may be set by the need to collect enough photons. In this situation, SAM is preferable to the HST. Its recent use with narrow-band filters and Fabry-Perot nicely illustrates this aspect.

Under good seeing, current AO instruments designed to work in the IR could provide substantial resolution gain in the red part of the visible spectrum, e.g. at Hα. However, their use at optical wavelengths is not envisioned and sometimes is impossible because of dichroics in the science path or the lack of optical instruments. This situation, presently to the advantage of SAM, is slowly evolving. The MUSE instrument at the VLT (Bacon et al. 2010) will operate with partial seeing correction at visible wavelengths over a $1'$ field using four sodium lasers. The ARGOS AO system at the LBT (Rabien et al. 2014) will implement GLAO with green Rayleigh

lasers and will work in the IR.

The potential of SAM will be fully exploited when its high spatial resolution is combined with spectroscopy. This is already happening when SAM is used with F-P. A multislit spectrometer for SAM is being developed by Robberto et al. (2016). This instrument, SAMOS, will use a commercial digital micromirror device (DMD) as a software-configurable multislit mask. The spectral resolution between 2000 and 8000 is envisioned. The SAMOS science targets are faint extragalactic and stellar objects where the increased spatial resolution brings a gain in sensitivity against the sky background, in addition to probing small spatial details and reducing source confusion.

The SAM instrument designed more than 10 years ago is technologically obsolete. Using modern electron multiplication CCD detectors with a fast gating, a higher-order wavefront sensing is feasible with the same laser power. If the DM is replaced by a new device with a larger actuator count, the increased compensation order will improve image correction at shorter wavelengths, in the green and blue spectral regions, bringing it closer to the SAM performance in the I band. Future upgrade of SAM along these lines will be decided based on its popularity and availability of funds.

REFERENCES

Andersen, D. R., Stoesz, J., Morris, S. et al. 2006, PASP, 118, 1574

Angel, J. R. P. & Lloyd-Hart, M. 2000, Proc. SPIE, 4007, 270

Bacon, R., Accardo, M., Adjali, L. et al. 2010, Proc. SPIE, 7735, 8

Baranec, C., Riddle, R., Ramaprakash, A. N. et al. 2012, Proc. SPIE, 8447, 4 (arXiv:1210.0532)

Fraga, L., Kunder, A., & Tokovinin, A. 2013, AJ, 145, 165

Hart, M., Milton, N. M., Baranec, C. et al. 2010, Nature, 466, 727

Law, N. M., Morton, T., Baranec, C. et al. 2014, ApJ, 791, 35

Mendez de Oliveira, C., Amram, P., Quint, B. et al. 2016, MNRAS, submitted.

Murphy, D. N. A. 2015, in IAU Symposium 309, p. 203

Olsen, K. A. G., Blum, R. D., & Rigaut, F. 2003, AJ, 126, 452

Rabien, S., Barl, L., Beckmann, U. et al. 2014, Proc. SPIE, 9148, 1

Rigaut, F., Salmon, D., Arsenault, R. et al. 1998, PASP, 110, 152

Rigaut, F., 2002, in: Beyond Conventional Adaptive Optics, eds. E. Vernet, R. Ragazzoni, S. Esposito, N. Hubin, ESO Conf. Workshop Proc. 58, ESO, Garching bei München, p. 11

Robberto, M., Donahue, M, Ninkov, Z. et al. 2016, Proc. SPIE, 9908, 99088V; doi:10.1117/12.2233094

Rutten, R., Blanken, M., McDermid, R. et al. 2006, NewAR, 49, 632

Salinas, R., Alabi, A., Richtler, T. & Lane, R. R. 2015, A&A, 577, 59

Salinas, R., Contreras Ramos, R., Strader, J. et al. 2016, AJ, accepted (arXiv:1605.06517).

Schmitt, J. R., Tokovinin, A., Wang, Ji et al. 2016, AJ, 151, 159 (ArXiv:1603.06945S).

Sebring, T. A., Krabbendam, V. L., & Heathcote, S. 2002, Proc. SPIE, 4837, 71

Thomas, S. 2004, Proc. SPIE, 5490, 766

Thomas, S., Fusco, T., Tokovinin, A. et al. 2006, MNRAS, 371, 323

Thompson, L. A. & Teare, S. W. 2002, PASP, 114, 1029

Tighe, R., Tokovinin, A., Schurter, P. et al. 2016, Proc. SPIE, 9908, 99803B; doi:10.1117/12.2233681

Tokovinin, A., 2004, PASP, 116, 941

Tokovinin, A. Gregory, B. & Schwarz, H., 2003, Proc. SPIE 4839, 673

Tokovinin, A., Thomas, S., Gregory, B. et al. 2004a, Proc. SPIE 5490, 870

Tokovinin, A., Thomas, S., & Vdovin, G. 2004b, Proc. SPIE, 5490, 580

Tokovinin, A. & Travouillon, T., 2006, MNRAS, 365, 1235

Tokovinin, A., 2008, Proc. SPIE 7015, 77

Tokovinin, A., Tighe, R., Schurter, P. et al. 2008, Proc. SPIE 7015, 157

Tokovinin, A., Tighe, R., Schurter, P. et al. 2010, Proc. SPIE, 7736, 132

Tokovinin, A., Tighe, R., Schurter, P. et al. 2012, Proc. SPIE, 8477, 166

Tokovinin, A., 2011, In: Second International Conference on Adaptive Optics for Extremely Large Telescopes, http://ao4elt2.lesia.obspm.fr

Tokovinin, A., 2013, In: Proceedings of the Third AO4ELT Conference. Simone Esposito and Luca Fini, eds. ISBN: 978-88-908876-0-4

Tokovinin, A. 2014, AJ, 148, 72